PAPER

Ionization cross sections of the Au L subshells by electron impact from the L_3 threshold to 100 keV

To cite this article: Suelen F Barros *et al* 2018 *J. Phys. B: At. Mol. Opt. Phys.* **51** 025201

View the article online for updates and enhancements.

Related content

IOP ebooks™

Bringing you innovative digital publishing with leading voices to create your essential collection of books in STEM research.

Start exploring the collection - download the first chapter of every title for free.

Ionization cross sections of the Au L subshells by electron impact from the L$_3$ threshold to 100 keV

Suelen F Barros[1] , **Vito R Vanin**[1], **Nora L Maidana**[1], **Marcos N Martins**[1], **Juan A García-Alvarez**[1], **Osvaldo C B Santos**[1], **Cleber L Rodrigues**[1], **Marina F Koskinas**[2] **and José M Fernández-Varea**[3,1]

[1] Instituto de Física, Universidade de São Paulo. Rua do Matão 1371, Cidade Universitária, CEP: 05508-090, São Paulo, SP, Brazil
[2] Instituto de Pesquisas Energéticas e Nucleares (IPEN/CNEN-SP). Av. Prof. Lineu Prestes 2242, Cidade Universitária, CEP: 05508-000, São Paulo, SP, Brazil
[3] Facultat de Física (FQA and ICC), Universitat de Barcelona. Diagonal 645, E-08028 Barcelona, Spain

E-mail: suelenb@if.usp.br

CrossMark

Abstract

We measured the cross sections for Au Lα, Lβ, Lγ, Lℓ and Lη x-ray production by the impact of electrons with energies from the L$_3$ threshold to 100 keV using a thin Au film whose mass thickness was determined by Rutherford Backscattering Spectrometry. The x-ray spectra were acquired with a Si drift detector, which allowed to separate the components of the Lγ multiplet lines. The measured Lα, Lβ, Lγ_1, L$\gamma_{2,3,6}$, L$\gamma_{4,4'}$, Lγ_5, Lℓ and Lη x-ray production cross sections were then employed to derive Au L$_1$, L$_2$ and L$_3$ subshell ionization cross sections with relative uncertainties of 8%, 7% and 7%, respectively; these figures include the uncertainties in the atomic relaxation parameters. The correction for the increase in electron path length inside the Au film was estimated by means of Monte Carlo simulations. The experimental ionization cross sections are about 10% above the state-of-the-art distorted-wave calculations.

(Some figures may appear in colour only in the online journal)

1. Introduction

Accurate cross sections for the ionization of atomic inner shells by electron impact are an important piece of information in the fundamental understanding of electron–atom collision processes as well as essential in many applied fields. An authoritative review of the experimental data available up to 2013 was published by Llovet *et al* [1]. It can be seen that there is much room for improvement in the accuracy of the measurements because the relative uncertainties are not better than 10%–20% (one standard deviation) for almost all studied elements, shells and electron energies.

In the case of Au L ionization and x-ray production cross sections, there is a considerable number of measurements [2–11]. The data from most of the experiments are restricted

either to the energy range from the L$_3$ threshold to 25–40 keV [2, 3, 6, 8–10], where the cross sections increase steeply and reach a broad maximum, or above 50 keV [5, 11], where they decrease smoothly while bremsstrahlung emission keeps growing. We have not found any data set obtained in a single experiment that covers the energy interval from the L$_3$ threshold to 100 keV.

Rahangdale *et al* [10] presented Au L$_1$, L$_2$ and L$_3$ ionization cross sections for energies between the L$_3$ ionization threshold and 40 keV. The behavior of their results is surprising. The cross sections for the ionization of the L$_3$ subshell are compatible with other experimental data and with the distorted-wave Born approximation (DWBA) [12, 13], which is one of the most reliable *ab initio* theoretical frameworks. The agreement worsens for the L$_2$ subshell, and for

L_1 their cross sections are inconsistent with other measurements and theoretical models.

In a recent paper, Pindzola [14] calculated Au L_i subshell ionization cross sections within the subconfiguration-average distorted-wave (SCADW) formalism, treating the transverse term of the electron–electron interaction without simplifications. The DWBA and SCADW predict essentially identical Au L_i ionization cross sections, which in the case of the L_1 subshell are roughly a factor of two larger than Rahangdale *et al*'s experimental values. Pindzola encouraged carrying out additional measurements to settle this issue [14].

Motivated by the aforementioned discrepancy we conducted new measurements of the Au ($Z = 79$) Lα, Lβ, Lγ, Lℓ and Lη x-ray production cross sections by electron impact with kinetic energies between the L_3 threshold and 100 keV. From these data we extracted the Au L_1, L_2 and L_3 subshell ionization cross sections. The present experiment improves upon our previous one [11] in several aspects: the energy range of the electron beam extends from the L_3 ionization threshold up to 100 keV; the x-ray production cross sections were determined by a direct method, with the thickness of the Au film estimated by Rutherford backscattering spectrometry (RBS), thus allowing to reduce the uncertainty of the results by about a factor of two with respect to our earlier work [11] and almost all reported experimental data [1]; the x-rays emitted by the irradiated target were detected by a Si drift detector (SDD), which performs better than Si(Li) spectrometers in the energy range of interest [11]; the beam current was measured, including the electrons scattered by the target; Monte Carlo simulations were done with the PENELOPE code [15] to estimate the effective path length of the electrons within the Au film for each incident beam energy. Our experimental cross sections were compared with the DWBA [12, 13] and SCADW [14] calculations and with available experimental data from the literature.

2. Experiment

Complete descriptions of the experimental arrangement and the beam line with details about the electron beam are going to be published elsewhere [16], hence we provide below a concise explanation of these characteristics only when relevant to this experiment.

2.1. Sample preparation and characterization

The physical vapor deposition technique was employed to deposit very thin films of Au on thin C backings. The substrates were prepared by evaporation of C onto a glass holder. Then they were detached from the glass and subsequently attached to the sample frame, a rectangle with 30 and 15 mm sides, 0.3 mm thick and a central hole 10 mm in diameter made of C fiber to minimize the production of photons by electrons in the beam halo or scattered by the target, which would yield undesired photoionization events. This framed backing was finally placed in an evaporator under vacuum, over a circular mask 8 mm in diameter, centered in the frame
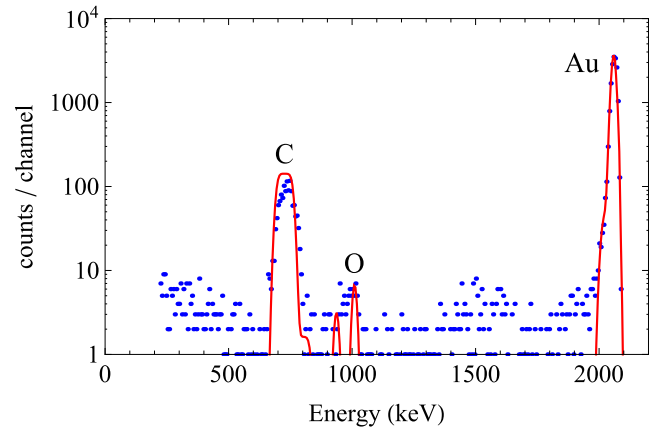

Figure 1. Experimental (dots) and simulated (line) RBS spectra pertaining to Au/C target #2 with the ^{4}He$^+$ beam hitting its center (case 2+ in figure 2). The energy dispersion is 6 keV/channel.

hole, to deposit a uniform Au film; this reduces the total amount of Au that could be hit by background photons in the irradiation chamber.

The mass thicknesses of the Au films and C substrates were estimated having recourse to RBS. To this end, the targets were irradiated with a 2200 keV ^{4}He$^+$ beam about 2 mm in diameter from the LAMFI Pelletron tandem accelerator [17], which impinged on the targets with an inclination of 7°. The energy spectra of the elastically backscattered ions were recorded by a surface barrier Si detector positioned at 120° with respect to the direction of the incident ion beam. The RBS spectra were analyzed with the SIMNRA [18] and MultiSIMNRA [19] codes. One of the collected energy spectra of backscattered ^{4}He particles is shown in figure 1 along with the SIMNRA simulated spectrum.

In order to quantify the uniformity of the Au films, four Au/C targets produced in the same batch were irradiated at three points: the target center, 2 mm above it and 2 mm below it. Figure 2 displays the measured mass thicknesses ρd (ρ is the mass density). The mass thickness of the Au film of target #2, the one chosen for the subsequent electron bombardment, was estimated as the average of the three RBS measurements performed on this target whereas its uncertainty was estimated based on the quadratic sum of the standard deviations of the mass thicknesses of all targets with the uncertainty deduced from the ^{4}He$^+$ spectrum fit procedure by MultiSIMNRA [19]. The resulting value is $\rho d = 9.6(5)\ \mu$g cm^{-2}. For the sake of completeness we quote the average mass thickness of the C backings, 9.2(4) μg cm^{-2}, although this quantity does not play any role in the data analysis below.

2.2. Irradiation chamber and detection system

The Au/C target #2 was positioned in the center of the cylindrical irradiation chamber, which has a diameter of 50 cm, making an angle $\alpha = 30°$ with the direction of the incident beam. The x-rays emitted at an angle of 90° with respect to the electron beam were detected by a SDD (Amptek, Bedford, USA). Its Si crystal has a nominal thickness of 0.5 mm and an area of 25 mm^2. The area of the

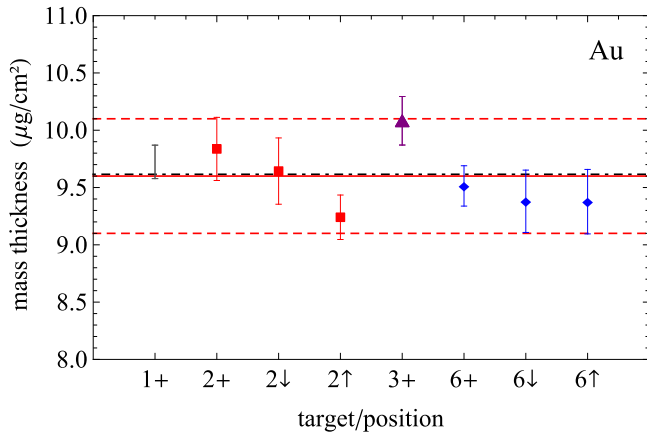J. Phys. B: At. Mol. Opt. Phys. **51** (2018) 025201

S F Barros *et al*

Figure 2. Mass thicknesses of the Au films in four Au/C targets, obtained by RBS. The abscissa identifies the target number and the irradiation point: $+$, $\downarrow$ and $\uparrow$ denote, respectively, the target center, 2 mm below it and 2 mm above it. The (red) squares belong to target #2; the continuous and dashed (red) horizontal lines are the adopted mass thickness and uncertainty for the Au film in this target (see the text). The (black) dot-dashed horizontal line is the average mass thickness of the Au films that ensues from the eight data points.

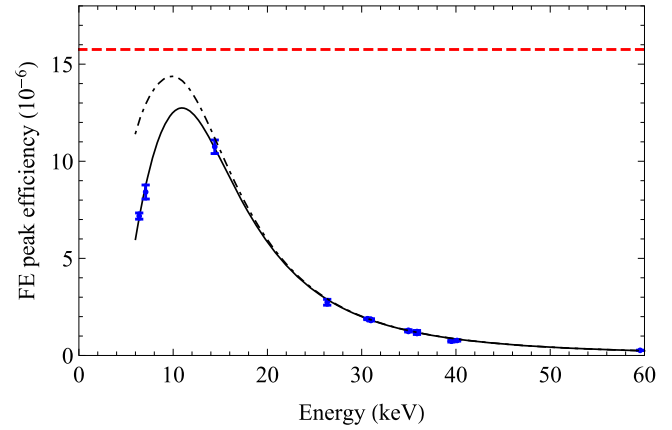**Figure 3.** FE peak efficiency, $\varepsilon_{FE}(E)$, of the SDD as a function of photon energy. The points are experimental values; the uncertainty bars correspond to one standard deviation. The continuous and dot-dashed curves are Seltzer's model [20] computed with the fitted values $\hat{L}$ and $\hat{\Omega}$ (see text) in the experimental conditions of the measurement with the radioactive sources (chamber filled with air) and with the electron beam (vacuum in chamber), respectively. The (red) horizontal dashed line indicates the geometrical efficiency $\hat{\Omega}/4\pi$.

internal collimator is 17 mm^2 and the 12.7 μm thick Be window is separated by 1.4 mm from the front surface of the active volume. The SDD was placed outside the vacuum chamber, 5 cm away from the spectroscopy window made of a Kapton foil and an Al foil with thicknesses of 25 μm and 5 μm, respectively. The base pressure in the vacuum chamber was 7×10^{-5} Pa during the experiment.

The full-energy (FE) peak efficiency curve of the SDD in the present setup, $\varepsilon_{FE}(E)$, was established by measuring γ-rays and characteristic x-rays emitted in the decay of ^{57}Co, ^{133}Ba, ^{152}Eu and ^{241}Am calibrated radioactive sources placed in the target position with the irradiation chamber filled with air. The sources were manufactured and their activities certified absolutely at the LMN-IPEN/CNEN-SP (Nuclear Metrology Laboratory, Research Institute and National Commission for Nuclear Energy, São Paulo). The carrier-free radioactive material was laid between two 7.5 μm thick Kapton foils, forming a spot 4 mm in diameter, and mounted in frames that are identical to those used for the targets. The Seltzer model [20] for the FE peak efficiency of this detector was carefully assessed in [21], and applied to compute $\varepsilon_{FE}(E)$ in this experiment. In particular, the Si crystal thickness L and the solid angle Ω were regarded as adjustable parameters. The fitted values were $\hat{L} = 0.497$ (6) mm and $\hat{\Omega} = 1.9798(14) \times 10^{-4}$ sr; the value of $\hat{L}$ is compatible with both the nominal thickness disclosed by the manufacturer and the estimate of 0.527(24) mm found in [21] for the same spectrometer. Figure 3 shows the experimental efficiency values obtained with the radioactive sources along with the FE peak efficiency calculated with these fitted parameters and the attenuating layers appropriate to the two experimental configurations employed in this work. Besides the detector and irradiation chamber windows, common to both configurations, we accounted for 30 cm of air and $(7.5 \, \mu\text{m})/\cos 60° = 15 \, \mu$m of Kapton when using the radioactive sources making an angle $\alpha = 30°$ with the direction of

the incident beam, and 5 cm of air when performing the measurements with the electron beam.

The beam current was evaluated from the sum of the charges collected in the Faraday cup, placed at 0° with respect to the beam line, and in the irradiation chamber, both electrically insulated.

2.3. Measurement of x-ray spectra

The irradiations were carried out at nineteen energies ranging from 13 to 100 keV, with some values chosen between the ionization thresholds of the L subshells. The energies and the respective uncertainties were estimated by fitting the tip of the bremsstrahlung spectra as described in [22]. The irradiation times spanned from 600 to 1800 s. The beam current was set between 600 nA and 2 μA so as to achieve a high counting statistics while keeping the SDD dead-time fraction smaller than 4%. The x-ray spectra depicted in figure 4 were acquired at 13.56(6) keV (only the L$_3$ subshell can be ionized), 14.35 (6) keV (now the L$_2$ subshell can be ionized too) and 16.16 (6) keV (the three subshell ionization channels are open). The spectra feature K x-ray peaks of Cr, Mn, Fe and Ni (5.4, 5.9, 6.4 and 7.5 keV, respectively) that originate from the ionization of the elements in the stainless steel wall of the irradiation chamber. Next to the Au M peaks, the K K and Ar K x-ray peaks (at 3.3 and 2.9 keV) are, respectively, due to traces of the soap used in the preparation of the C backing and the air between the detector and the chamber spectroscopy window.

3. Data analysis

3.1. X-ray peak area estimate

Each x-ray peak was fitted with a Voigt function [21], and a flat shelf was added to account for photoelectron escape and
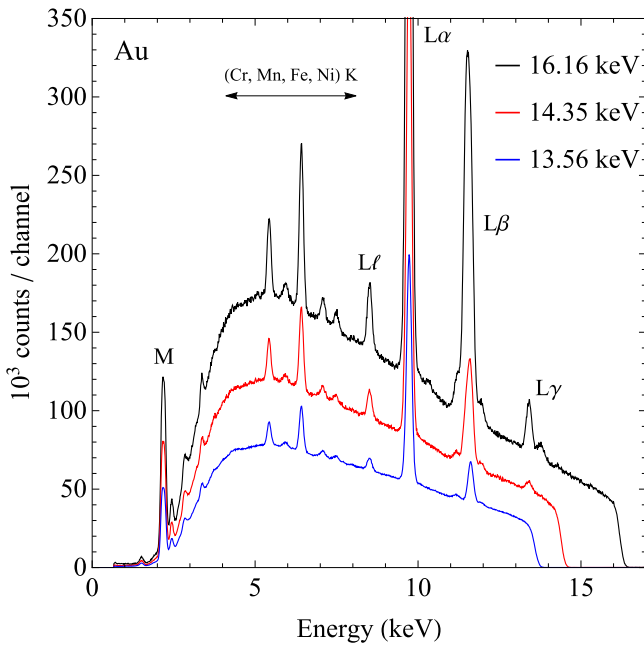
Figure 4. Energy spectra of the x-rays emitted by the Au/C sample in the runs with 13.56(6) keV, 14.35(6) keV and 16.16(6) keV electrons (bottom to top). The energy dispersion is 13 eV/channel. The Cr, Mn, Fe and Ni K x-rays originate in the wall of the irradiation chamber.

other secondary detection effects. In the Voigt function, the natural width Γ was borrowed from the compilation of Krause and Oliver [23]. The flat shelf was convolved with the Gaussian that models the pulse broadening of the detection system, and its amplitude h was kept fixed based on the model proposed by Scholze and Procop [24]. The Gaussian dispersion associated with the detector response as a function of the photon energy E was given by $s(E) = \sqrt{s_{el}^2 + W_{Si} F_{Si} E}$ [20], where W_{Si} and F_{Si} are, respectively, the average energy expended in the formation of an electron–hole pair in Si and the Fano factor [25]. The parameter s_{el} that corresponds to electronic noise associated with the pulse amplification process was adjusted in each run whereas the product $W_{Si} F_{Si}$ was fixed to the value found during the calibration previously done with radioactive sources. The other fitted parameters were peak positions and areas, and those that model the spectrum continuous component, as described below.

The parameters of the Lα and Lγ multiplets and those of the Lℓ and Lη lines were fitted concomitantly by the least-squares procedure, hence the high counting statistics of the Lα doublet was preponderant in the estimate of the peak widths. In the Lα doublet region, three peaks were included to fit the Lα_1 and Lα_2 lines and a small shoulder that was observed on the right side of the Lα_1 peak (see below). In turn, in the Lγ group, six peaks were included for the Lγ_1, Lγ_2, Lγ_3, L$\gamma_{4,4'}$, Lγ_5 and Lγ_6 lines.

In each group, we left the position n_{line} of a single line as a free parameter and held the positions of the others fixed relative to it, adopting the experimental x-ray energies recommended by Deslattes *et al* [26]. The positions of the Lℓ and Lη lines were left free in the fit. The peak areas were

regarded as free parameters except for the Lγ_6 peak, whose area was fixed with respect to that of Lγ_1 taking as reference Scofield's emission rates [27].

The continuous component of the spectrum was modeled as the sum of a polynomial of the second degree with a constant that multiplies the form of the bremsstrahlung spectrum generated by the target. A theoretical model of doubly differential bremsstrahlung cross section [28–30] was fitted to the energy region of the tip of each of the experimental spectra following the procedure described in [22], which also allowed to determine the mean energy of the incident electron beam.

The expression employed in the fit procedure was

$$y(n) = \sum_{i=1}^{M} A_i\, V(n_i, s(E(n_i)), \Gamma_i; n) + \phi(n), \qquad (1)$$

where V is the Voigt function, A_i and n_i are the areas and positions (channels) of the M peaks included in the fit, respectively. The function ϕ models the continuous component of the spectrum; it is given by

$$\phi(n) = c_0 + c_1(n - n_0) + c_2(n - n_0)^2 + k\, B(E(n)), \quad (2)$$

being c_j the coefficients of the 2nd degree polynomial and k a constant that multiplies the bremsstrahlung spectrum $B(E(n))$. The arbitrary constant n_0 (not an adjustable parameter) was set as the central channel in the region of interest; this choice strongly reduces the statistical correlation between the fitted parameters c_j. The experimental spectrum for a 30 keV electron beam is plotted in figure 5(a) together with the fitted lines and figure 5(b) displays the corresponding standardized fit residuals. The reduced χ^2 for this fit was 1.3.

It was not possible to separate the lines in the Lβ group with sufficient accuracy to determine the cross section in the 13–100 keV energy range owing to their strong overlap. Consequently we estimated the area of the complete group by summing the number of counts in the corresponding energy region and subtracting the counts of the continuum component, which was deduced from the simultaneous fit of the Lα and Lγ multiplets.

The area of the Lα doublet was estimated by summing Lα_1 and Lα_2 fitted areas, and that of the Lγ group, by the sum of Lγ_1, Lγ_2, Lγ_3, L$\gamma_{4,4'}$, Lγ_5 and Lγ_6 fitted areas. In both cases, the covariances between the area parameters from the least-squares fit procedure were incorporated in the evaluation of the uncertainties.

In all spectra, we observed a small shoulder at the right side of the Lα doublet. Unfortunately, we could not ascertain whether it was a satellite line, a transition which is forbidden in the dipole approximation or some secondary detection effect. However, when the target was irradiated by an electron beam whose energy was lower than the Au L$_3$ ionization threshold, we did not observe a peak in this region, and therefore we concluded that it was not due to contamination by another element. The area of the peak fitted to reproduce the shoulder is about half of the Lη area, and therefore it did not compromise the measurement of the Lα doublet area within the stated uncertainties. Nevertheless, it is very close to the Lη line and may have affected the estimate of its area.
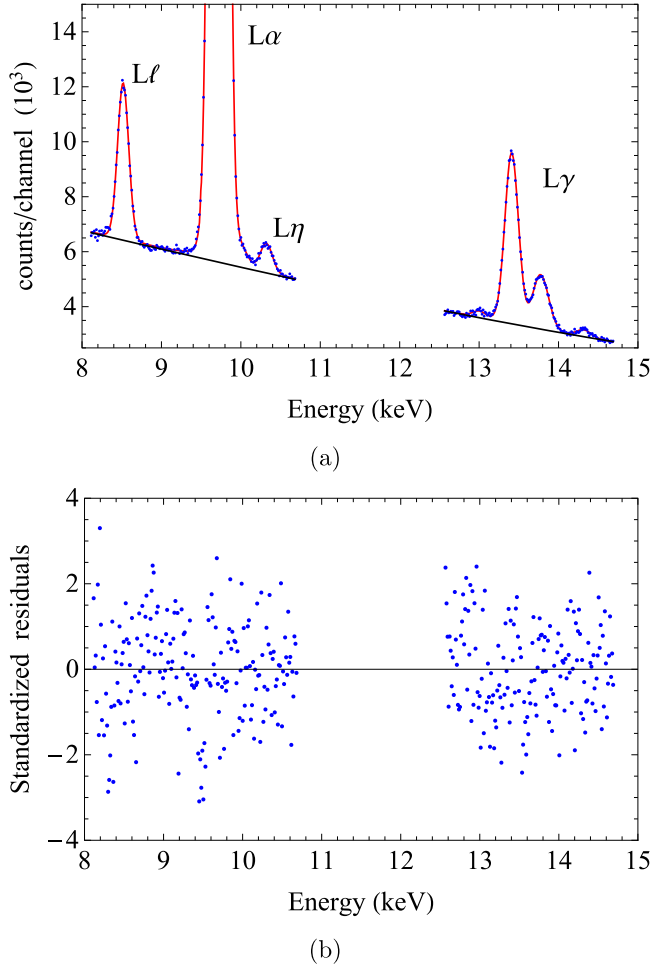
J. Phys. B: At. Mol. Opt. Phys. **51** (2018) 025201

S F Barros *et al*

(a)

(b)

Figure 5. (a) Model function (red curve) calculated with the fitted parameters and experimental points of the Lα and Lγ multiplets as well as the Lℓ and Lη lines for the spectrum recorded at 30 keV. The black curve is the continuous component ϕ, equation (2). (b) Standardized fit residuals of the data points in (a).

From the comparison of the current data with the ratio of Lη and Lγ_1 intensities reported by Scofield [27], we think that about 10(5)% of the Lη area was lost. Hence, we decided to multiply the fitted Lη peak area by 1.10(5) and make the corresponding uncertainty propagation.

3.2. X-ray production cross sections

When an electron beam penetrates a self-sustaining film of a given element following a straight trajectory and without loss of energy, the x-ray production cross section σ_{Lj}^x for the peak Lj in the run with electrons of energy E can be evaluated from

$$\sigma_{Lj}^x(E) = \frac{N_{Lj}}{N_e(\mathcal{N}d/\cos\alpha)\varepsilon_{FE}(E_{Lj})}, \quad (3)$$

where N_{Lj} is the area of the Lj peak (energy E_{Lj}), $\mathcal{N}$ is the number of Au atoms per unit volume, d is the thickness of the film, α is the angle of inclination of the target with respect to the beam, and N_e is the number of incident electrons. In equation (3) the emission of characteristic L x-rays is assumed to be isotropic even if these originate from vacancies in the L$_3$

subshell. The correction for the dead time of the acquisition system was implemented according to [31, 32].

Electrons that hit a target undergo inelastic and elastic collisions that change their energy and direction of propagation. In particular, the effective path length of the electron beam within the Au film will be slightly longer than $d/\cos\alpha$. Monte Carlo simulations with the PENELOPE [15] code yielded an energy-dependent multiplicative correction factor that accounts for this path length increase. Figure 6 shows the simulated correction factor for the Au film with $\rho d = 9.6(5)\,\mu\mathrm{g\,cm^{-2}}$ and $\alpha = 30°$ as a function of the energy of the incident electron beam.

The x-ray production cross sections of the Lα, Lβ and Lγ multiplets and the Lℓ and Lη lines were calculated from expression (3) with the values of N_e, $\mathcal{N}d$ and $\varepsilon_{FE}(E_{Lj})$ estimated as described above. The uncertainty of these cross sections was found by the usual propagation method applied to equation (3).

3.3. L-subshell ionization cross sections

We derived the Au L$_1$, L$_2$ and L$_3$ subshell ionization cross sections employing the methodology presented in [11], but with a larger number of x-ray lines. As it was possible to acquire spectra with high statistic and good resolution, L$\gamma_{4,4'}$ and Lγ_5, which could not be considered previously [11], were fitted and included in the analysis. In short, the groups and lines selected here to find σ_{L_1}, σ_{L_2} and σ_{L_3} were Lα, Lβ, Lγ_1, L$\gamma_{2,3,6}$, L$\gamma_{4,4'}$, Lγ_5, Lℓ and Lη. The corresponding x-ray production cross sections are connected to the L$_i$ subshell ionization cross sections through the vacancy-production cross sections $\sigma_{L_i}^h$ by the relations

$$\sigma_{L\alpha}^x = \frac{\Gamma_{L_3M_{4,5}}}{\Gamma_{3,tot}}\,\omega_3\,\sigma_{L_3}^h, \quad (4)$$

$$\sigma_{L\beta}^x = \frac{\Gamma_{1\beta}}{\Gamma_{1,tot}}\,\omega_1\,\sigma_{L_1}^h + \frac{\Gamma_{2\beta}}{\Gamma_{2,tot}}\,\omega_2\,\sigma_{L_2}^h + \frac{\Gamma_{3\beta}}{\Gamma_{3,tot}}\,\omega_3\,\sigma_{L_3}^h, \quad (5)$$

$$\sigma_{L\gamma_1}^x = \frac{\Gamma_{L_2N_4}}{\Gamma_{2,tot}}\,\omega_2\,\sigma_{L_2}^h, \quad (6)$$

$$\sigma_{L\gamma_{2,3,6}}^x = \frac{\Gamma_{L_1N_{2,3}}}{\Gamma_{1,tot}}\,\omega_1\,\sigma_{L_1}^h + \frac{\Gamma_{L_2O_4}}{\Gamma_{2,tot}}\,\omega_2\,\sigma_{L_2}^h, \quad (7)$$

$$\sigma_{L\gamma_{4,4'}}^x = \frac{\Gamma_{L_1O_{2,3}}}{\Gamma_{1,tot}}\,\omega_1\,\sigma_{L_1}^h, \quad (8)$$

$$\sigma_{L\gamma_5}^x = \frac{\Gamma_{L_2N_1}}{\Gamma_{2,tot}}\,\omega_2\,\sigma_{L_2}^h, \quad (9)$$

$$\sigma_{L\ell}^x = \frac{\Gamma_{L_3M_1}}{\Gamma_{3,tot}}\,\omega_3\,\sigma_{L_3}^h, \quad (10)$$

$$\sigma_{L\eta}^x = \frac{\Gamma_{L_2M_1}}{\Gamma_{2,tot}}\,\omega_2\,\sigma_{L_2}^h, \quad (11)$$

where ω_i is the fluorescence yield of subshell L$_i$, $\Gamma_{i\beta}$ are the emission rates for transitions belonging to the Lβ group, $\Gamma_{L_i(M,N,O)_j}$ is the emission rate for the transition L$_i$(M,N,O)$_j$, and $\Gamma_{i,tot}$ is the sum of the emission rates for all possible transitions to the L$_i$ subshell.

J. Phys. B: At. Mol. Opt. Phys. **51** (2018) 025201

S F Barros *et al*

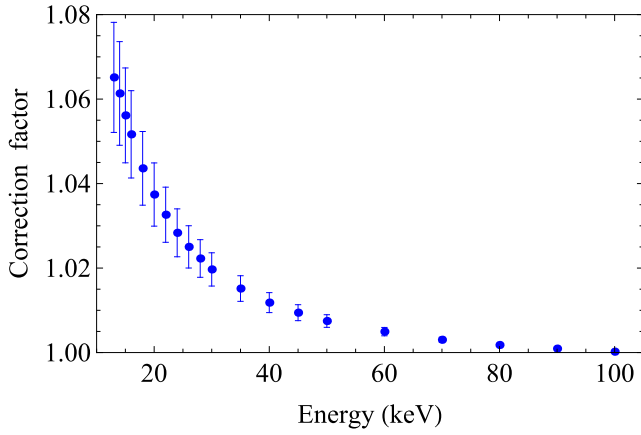**Figure 6.** Multiplicative correction factor to determine the effective path length of electrons that impinge with $\alpha = 30°$ on the 9.6(5) μg cm^{-2} thick Au film as a function of the incident beam energy.

The vacancy-production cross sections are in turn related to the K and L$_i$ (sub)shell ionization cross sections by means of expressions

$$\sigma_{L_1}^h = \sigma_{L_1} + \eta_{KL_1}\,\sigma_K, \tag{12}$$

$$\sigma_{L_2}^h = \sigma_{L_2} + f_{12}\,\sigma_{L_1} + (\eta_{KL_2} + f_{12}\,\eta_{KL_1})\,\sigma_K, \tag{13}$$

$$\sigma_{L_3}^h = \sigma_{L_3} + f_{23}\,\sigma_{L_2} + (f_{13} + f'_{13} + f_{12}\,f_{23})\,\sigma_{L_1}$$
$$+ (\eta_{KL_3} + f_{23}\,\eta_{KL_2} + (f_{13} + f'_{13} + f_{12}\,f_{23})\eta_{KL_1})\,\sigma_K, \tag{14}$$

where σ_K, σ_{L_1}, σ_{L_2} and σ_{L_3} are, respectively, the K, L$_1$, L$_2$ and L$_3$ (sub)shell ionization cross sections by electron impact, f_{ij} are the Coster–Kronig non-radiative transition probabilities, f'_{13} is the Coster–Kronig radiative transition probability and η_{KL_i} are the vacancy-transfer probabilities from the K-shell to the L$_i$ subshells. The contribution of intrashell radiative transitions from L$_1$ to L$_2$ have not been included in equations (13) and (14) because the corresponding yield f'_{12} is extremely small.

As described in [11], the x-ray production cross sections in expressions (4)–(11) are linear in the ionization cross sections. Thus, they can be written in the matrix form
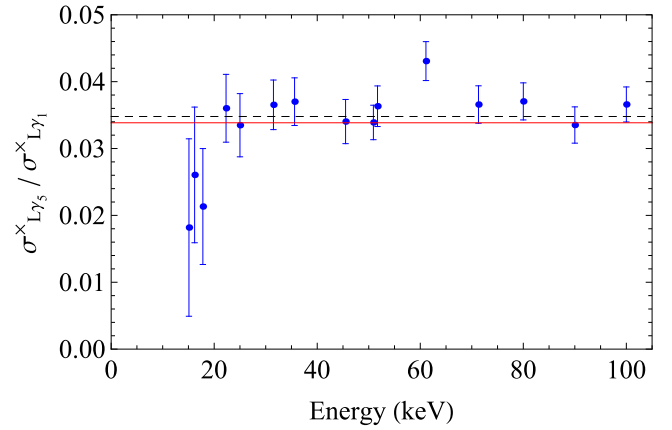
$$\boldsymbol{\sigma}_0^x = \mathbb{X}\,\boldsymbol{\sigma}_0, \tag{15}$$

where $\boldsymbol{\sigma}_0^x$ and $\boldsymbol{\sigma}_0$ are the column vectors with the true values of the cross sections for x-ray production and L-subshell ionization, respectively, and $\mathbb{X}$ is the design matrix. Taking the experimental data $\boldsymbol{\sigma}_{exp}^x$ as estimates of $\boldsymbol{\sigma}_0^x$, with covariance matrix $\mathbb{V}_{\sigma_{exp}^x}$, the least-squares estimate for $\boldsymbol{\sigma}_0$ is given by [11, 33]

$$\hat{\boldsymbol{\sigma}} = (\mathbb{X}^T\,\mathbb{V}_{\sigma_{exp}^x}^{-1}\,\mathbb{X})^{-1}\mathbb{X}^T\,\mathbb{V}_{\sigma_{exp}^x}^{-1}\,\boldsymbol{\sigma}_{exp}^x. \tag{16}$$
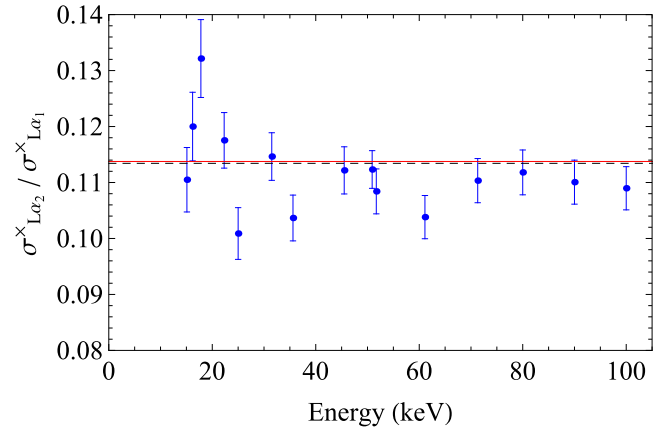
(a)

(b)

Figure 7. Experimental ratios (a) $\sigma_{L\alpha_2}^x/\sigma_{L\alpha_1}^x$ and (b) $\sigma_{L\gamma_5}^x/\sigma_{L\gamma_1}^x$ for Au by electron impact. The horizontal lines indicate the ratios tabulated by Scofield [27] (black dashed line) and by Campbell and Wang [37] (red continuous line).

The atomic relaxation parameters in the design matrix $\mathbb{X}$ have uncertainties that must be propagated to the variances of the fitted parameter vector. A good approximation for the total variance of $\hat{\boldsymbol{\sigma}}$ is [11]

$$\mathbb{V}_{\hat{\boldsymbol{\sigma}}} = (\mathbb{X}^T\,\mathbb{V}_{\sigma_{exp}^x}^{-1}\,\mathbb{X})^{-1} + \mathbb{D}\,\mathbb{V}_{par}\,\mathbb{D}^T, \tag{17}$$

where the first and second terms in the right-hand side account for the uncertainties in the experimental x-ray production cross sections and atomic relaxation parameters, respectively. $\mathbb{V}_{par}$ is the variance matrix of the relaxation parameters and $\mathbb{D}$ is a rectangular matrix whose elements are the derivatives of the (sub) shell ionization cross sections with respect to each of these parameters.

It is important to remember that when the energy of the electron beam is greater than the K-shell binding energy ($U_{Au\,K} = 80.7$ keV [26]), migration of a K-shell vacancy to any L-subshell must be considered. In this experiment, for 90 and 100 keV electron beams, the K-shell ionization cross section $\hat{\sigma}_K$ was added to the vector $\hat{\boldsymbol{\sigma}}$ of parameters to be fitted, and the column vector $\boldsymbol{\sigma}_{exp}^x$ should be augmented with

Table 1. Measured Lα, Lβ, Lγ, Lℓ and Lη x-ray production cross sections of Au by electron impact. The numbers between parentheses are the uncertainties (one standard deviation) in units of the least significant digit.

E (keV)	$\sigma^x_{L\alpha}$ (b)	$\sigma^x_{L\beta}$ (b)	$\sigma^x_{L\gamma}$ (b)	$\sigma^x_{L\ell}$ (b)	$\sigma^x_{L\eta}$ (b)
12.98(6)	34(2)	8.0(5)		1.62(11)	
13.56(6)	51(3)	11.3(7)		2.44(15)	
13.60(7)	52(3)	11.3(7)		2.62(16)	
14.35(6)	71(4)	22.9(14)	1.71(11)	3.46(21)	
15.08(7)	90(5)	37.4(22)	5.2(3)	4.37(27)	0.38(18)
16.16(6)	111(7)	56(3)	8.0(5)	5.4(3)	0.79(25)
17.85(8)	138(8)	78(5)	11.7(7)	6.7(4)	1.0(3)
22.45(7)	173(10)	108(6)	17.4(10)	8.5(5)	1.8(4)
25.01(8)	183(11)	117(7)	19.2(11)	9.0(5)	1.8(4)
31.62(7)	194(11)	129(8)	21.1(12)	9.6(6)	2.0(4)
35.53(8)	194(11)	131(8)	21.8(13)	9.6(6)	2.1(4)
45.42(4)	191(11)	131(8)	21.7(13)	9.5(6)	2.1(4)
50.88(13)	186(11)	128(7)	21.5(13)	9.2(6)	2.0(4)
51.70(4)	184(11)	127(7)	21.1(12)	9.1(5)	1.9(4)
60.98(5)	175(10)	123(7)	20.4(12)	8.6(5)	1.8(4)
71.30(4)	166(10)	117(7)	19.4(11)	8.2(5)	1.8(4)
80.55(6)	159(9)	112(7)	19.1(11)	7.9(5)	1.7(3)
90.06(8)	152(9)	107(6)	18.1(11)	7.6(5)	1.7(3)
100.15(9)	148(8)	105(6)	18.0(10)	7.4(4)	1.7(3)

Table 2. Au L_1, L_2 and L_3 subshell ionization cross sections. The numbers in parentheses represent the uncertainty associated with the value (one standard deviation).

E (keV)	σ_{L_1} (b)	σ_{L_2} (b)	σ_{L_3} (b)
12.98(6)			139(7)
13.56(6)			203(10)
13.60(7)			210(11)
14.35(6)		27(2)	279(16)
15.08(7)	38(4)	56(4)	328(20)
16.16(6)	57(6)	91(7)	400(26)
17.85(8)	86(8)	134(10)	488(32)
22.45(7)	132(11)	199(14)	598(41)
25.01(8)	152(12)	215(15)	624(44)
31.62(7)	163(12)	242(17)	663(47)
35.53(8)	168(13)	249(17)	658(47)
45.42(4)	168(12)	246(17)	647(46)
50.88(13)	174(12)	240(16)	625(45)
51.70(4)	175(12)	237(16)	613(44)
60.98(5)	169(12)	236(16)	579(42)
71.30(4)	160(11)	219(15)	555(40)
80.55(6)	149(10)	217(14)	532(39)
90.06(8)	143(10)	204(14)	510(37)
100.15(9)	141(10)	205(13)	495(36)

measured $K\alpha_{1,2}$ and $K\beta_{1,3}$ x-ray production cross sections deduced from the corresponding peak areas. However, the SDD employed in these measurements has an efficiency for the Au Kα and Kβ x-rays ($E_{K\alpha_{1,2}}$= 68.1 keV, $E_{K\beta_{1,3}}$= 77.3 keV) that is very small and prevents a proper observation of the peaks. Therefore, for these two beam energies we took x-ray emission cross sections interpolating between the experimental data published in [22]; the adopted values of

$\sigma^x_{K\alpha_{1,2}}$ and $\sigma^x_{K\beta_{1,3}}$ were 1.38 b and 0.30 b for 90.06 keV and 2.45 b and 0.51 b for 100.15 keV, respectively.

Ionization cross sections were calculated with atomic relaxation parameters which consist in: fluorescence yields and Coster–Kronig coefficients given by Kolbe *et al* [34]; radiative and non-radiative vacancy-transfer probabilities from the K-shell to the L_i subshells calculated by Scofield [35] and Rao [36], respectively, and x-ray emission rates tabulated by Campbell and Wang [37]. The transfer probabilities from [35] have uncertainties of the order of 2% [38] and the fraction of the Auger contribution in η_{KL_i} introduces an uncertainty around 15% [36].

4. Results

Figure 7 compares the experimental ratios $\sigma^x_{L\alpha_2}/\sigma^x_{L\alpha_1}$ and $\sigma^x_{L\gamma_5}/\sigma^x_{L\gamma_1}$ to the ratios of emission rates tabulated in [27, 37]. Table 1 lists our experimental Lα, Lβ, Lγ, Lℓ and Lη x-ray production cross sections derived from equation (3). Figure 8 displays the present measurements together with experimental values previously reported by other authors [5, 6, 8–11] and with theoretical x-ray production cross sections evaluated within the DWBA [12, 13].

Table 2 collects the results for Au L_1, L_2 and L_3 subshell ionization cross sections and their respective uncertainties. The procedure described at the end of section 3.1 to correct the Lη areas has a negligible influence on the estimate of the Au L_2 ionization cross section, which is dominated by the $L\gamma_1$ and some Lβ lines. Figure 9 compares these cross sections with other experimental data [2–7, 10, 11] and the predictions of the DWBA [12, 13] and SCADW [14] formalisms.
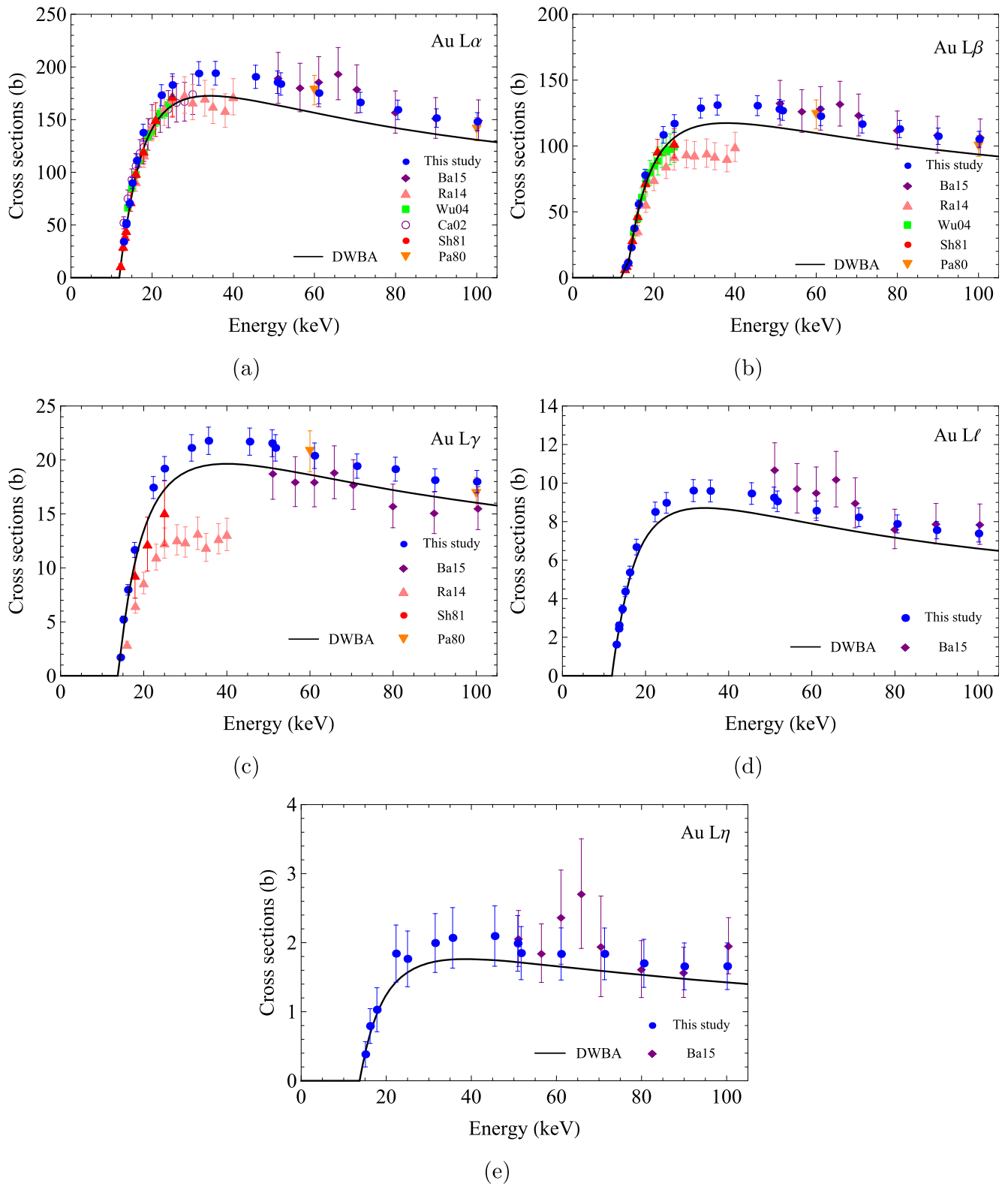
7

Figure 8. Au Lα, Lβ, Lγ, Lℓ and Lη x-ray production cross sections. The (blue) circles are the experimental values from this work. (Orange) inverted triangles, (red) circles, (purple) empty circles, (green) squares, (pink) triangles and (purple) diamonds represent the data from references Pa80 [5], Sh81 [6], Ca02 [8], Wu04 [9], Ra14 [10] and Ba15 [11], respectively. The continuous curves are the theoretical DWBA cross sections [12, 13].

5. Discussion

A thorough review of the Au L x-ray production and ionization cross section measurements in the literature can be found in [11] and will not be repeated here.

The x-ray production cross sections can be estimated by two different methods, and here we adopt the same definitions as in [11]. We shall call *direct measurement* that where N_e is obtained measuring the beam current, and the sample mass thickness is determined by any independent experimental procedure. The name *relative method* will mean that the product $N_e d$ is deduced in the same experiment from the bremsstrahlung yield and its accepted theoretical differential cross section.

In this work we used a multiplet decomposition procedure, with the simultaneous fit of all parameters of the $L\ell$ and $L\eta$ lines and of the $L\alpha$ and $L\gamma$ groups, which differs from that employed in [11], where the $L\alpha$ and $L\gamma$ multiplet parameters were fitted separately. The standardized residuals of the fit pertaining to the x-ray spectrum acquired for the 30 keV electron beam, figure 5(b), attest to the good quality of the fit. When the parameters of the $L\gamma$ multiplet are fitted separately from those of the $L\alpha$ doublet, the parameter s_{el} (the component of the peak width caused by electronic noise) may not be well estimated owing to the strong overlap of the lines in this multiplet, leading to an underestimation of the peak areas. This problem disappears when $L\alpha$ and $L\gamma$ are fitted simultaneously because the high statistic of the $L\alpha$ doublet is preponderant in the estimate of s_{el}. This change in fit methodology led to a small increase of around 13% in the present $L\gamma$ peak areas compared to those of [11] and explains most of the difference in the corresponding x-ray emission cross section (see figure 8(c)).

The $\sigma^x_{L\alpha_2}/\sigma^x_{L\alpha_1}$ ratios plotted in figure 7 confirm that the $L\alpha_1$ and $L\alpha_2$ lines were well separated in the fit. In addition, the $\sigma^x_{L\gamma_5}/\sigma^x_{L\gamma_1}$ ratios show that the spectra had sufficient counting statistics to distinguish the $L\gamma_5$ line from the continuous component and fit the peak area with good precision.

The Au L x-ray production cross sections reported here are the first ones obtained by *direct measurement* using the Microtron and LAMFI Pelletron tandem accelerators at the Universidade de São Paulo. With respect to our previous 50–100 keV cross sections resulting from a relative measurement, they are in complete agreement for the $L\alpha$ and $L\beta$ multiplets and display for $L\gamma$ small differences caused by the change in the fit methodology.

The new x-ray production cross sections have uncertainties of the order of 6% for the $L\alpha$, $L\beta$ and $L\gamma$ multiplets and around 6% and 25% for the $L\ell$ and $L\eta$ lines, which constitutes a substantial improvement in the accuracy compared to the data we measured earlier [11], where these uncertainties were about 13%, 15% and 30%, respectively. This improvement is mainly a consequence of the *direct measurement* used to obtain the x-ray production cross sections, which reduced the uncertainty in the Au film thickness from 11% to 5%. Thereby, the relative uncertainties in the Au L_1, L_2 and L_3 subshell ionization cross sections are approximately 8%, 7% and 7%, respectively, making the present results arguably the most precise data set in the literature.
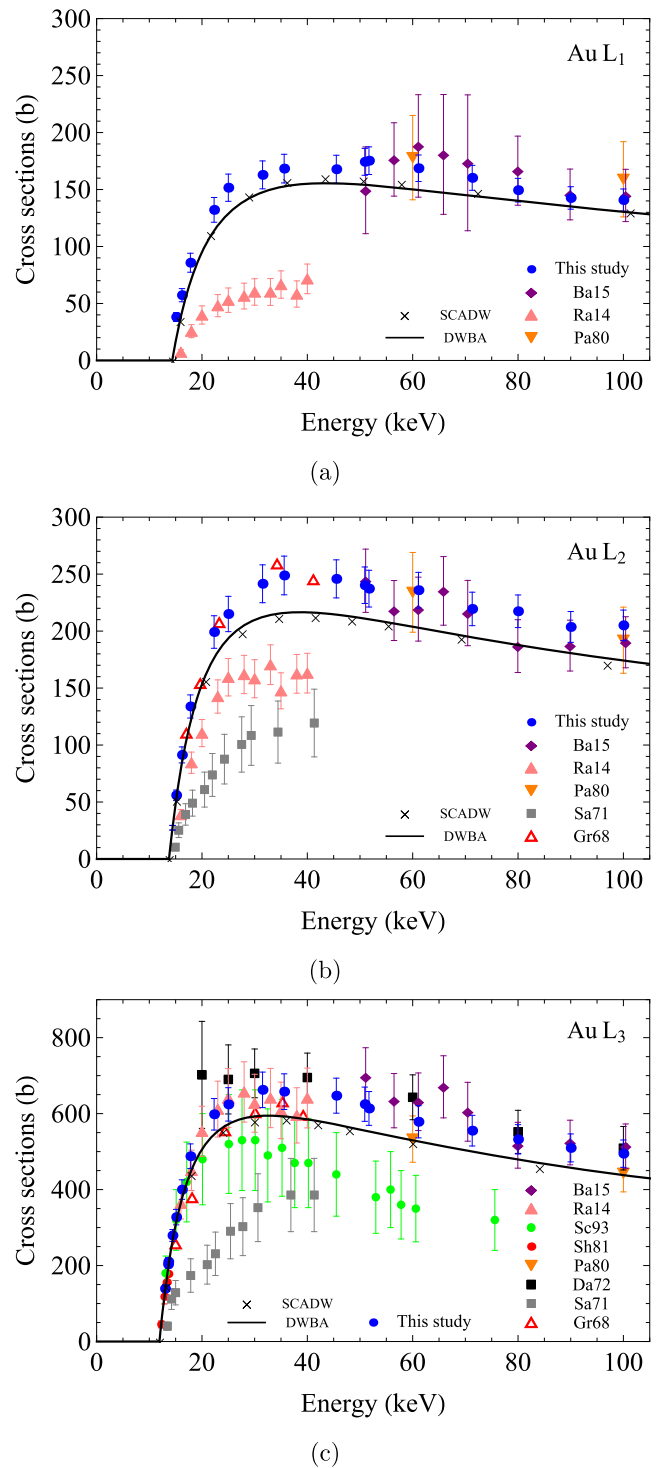

Figure 9. Au L_1, L_2 and L_3 subshell ionization cross sections. The (blue) circles are the experimental values from this work. (Red) empty triangles, (gray) squares, (black) squares, (orange) inverted triangles, (red) circles, (green) circles, (pink) triangles and (purple) diamonds represent the data from references Gr68 [2], Sa71 [3], Da72 [4], Pa80 [5], Sh81 [6], Sc93 [7], Ra14 [10] and Ba15 [11], respectively. The continuous curves and the crosses are the predictions of the *ab initio* DWBA [12, 13] and SCADW [14] formalisms, respectively.

Compared to theoretical calculations, the $L\alpha$, $L\beta$ and $L\gamma$ x-ray production cross sections reported here are about 10%–12% higher than the predictions of the DWBA and SCADW formalisms, while the experimental Au L_1, L_2 and L_3 subshell

J. Phys. B: At. Mol. Opt. Phys. **51** (2018) 025201

S F Barros *et al*

ionization cross sections are around 10% above the DWBA and SCADW values for electron energies a few keV above of the ionization threshold.

It is well known that x-rays emitted by the filling of vacancies in the L_3 subshell present an anisotropic angular distribution [39]. The atomic alignment produced by electron impact is appreciable near the ionization threshold but decreases very rapidly with increasing energy. Calculations done within the Born approximation conclude that the alignment parameter in Au is about 12% at 12 keV. The ensuing x-ray anisotropy is, however, attenuated by a factor that depends on the angular momentum of the subshell to which the vacancy is transferred. For the $L\alpha_1$ and $L\ell$ lines this factor is $1/10$ and $1/2$, respectively [39], which yields an effective anisotropy in the emission of these lines around 1.2% for $L\alpha_1$ and 6% for $L\ell$ (at 12 keV). Since the measured L_3 ionization cross section is dominated by the observed $L\alpha_1$ peak area (which is some 17 times larger than that of the $L\ell$ peak) and the uncertainty of our σ_{L_3} cross sections is 6%, the assumption of isotropic emission can cause errors about $1/5$ of the stated uncertainty close to the threshold; for increasing energies the errors are even smaller.

6. Conclusions

We have measured Au $L\alpha$, $L\beta$, $L\gamma$, $L\ell$ and $L\eta$ x-ray production and L_1, L_2 and L_3 subshell ionization cross sections by electron impact for energies from the L_3 threshold up to 100 keV. The uncertainties of the present cross sections are significantly smaller than those of our previous experiment, which was conducted using the relative method for energies between 50 and 100 keV, but otherwise both data sets are fully consistent.

Our results are in reasonable agreement with most of the other experimental works and slightly above the theoretical DWBA and SCADW formalisms. To the best of our knowledge, this corresponds to the first results of the Au L cross sections by electron impact performed from the L_3 ionization threshold up to 100 keV in a single experiment, and the most precise in this energy range to date.

ORCID iDs

Suelen F Barros ⦿ https://orcid.org/0000-0001-5683-175X

References

[1] Llovet X, Powell C J, Salvat F and Jablonski A 2014 *J. Phys. Chem. Ref. Data* **43** 013102
[2] Green M and Cosslett V E 1968 *J. Phys. D: Appl. Phys.* **1** 425
[3] Salem S I and Moreland L D 1971 *Phys. Lett.* **37A** 161
[4] Davis D V, Mistry V D and Quarles C A 1972 *Phys. Lett.* **38A** 169
[5] Pálinkás J and Schlenk B 1980 *Z. Phys.* A **197** 29
[6] Shima K, Nakagawa T, Umetani K and Mikumo T 1981 *Phys. Rev.* A **24** 72
[7] Schneider H, Tobehn I, Ebel F and Hippler R 1993 *Phys. Rev. Lett.* **71** 2707
[8] Campos C S, Vasconcellos M A Z, Llovet X and Salvat F 2002 *Phys. Rev.* A **66** 012719
[9] Wu Y, An Z, Liu M T, Duan Y M, Tang C H and Luo Z M 2004 *J. Phys. B: At. Mol. Opt. Phys.* **37** 4527
[10] Rahangdale H V, Guerra M, Das P K, De S, Santos J P, Mitra D and Saha S 2014 *Phys. Rev.* A **89** 052708
[11] Barros S F, Vanin V R, Maidana N L and Fernández-Varea J M 2015 *J. Phys. B: At. Mol. Opt. Phys.* **48** 175201
[12] Bote D and Salvat F 2008 *Phys. Rev.* A **77** 042701
[13] Llovet X, Salvat F, Bote D, Salvat-Pujol F, Jablonski A and Powell C J 2014 *NIST Database of Cross Sections for Inner-Shell Ionization by Electron or Positron Impact, Version 1.0* NIST Standard Reference Database 164 (https://doi.org/10.6028/NIST.NSRDS.164)
[14] Pindzola M S 2015 *J. Phys. B: At. Mol. Opt. Phys.* **48** 015201
[15] Salvat F, Fernández-Varea J M and Sempau J 2011 *PENELOPE-2011: A Code System for Monte Carlo Simulation of Electron and Photon Transport* (Issy-les-Moulineaux: OECD/NEA) (https://oecd-nea.org/science/docs/2011/nsc-doc2011-5.pdf Accessed: 23 November 2017)
[16] Vanin V R, Maidana N L, Mangiarotti A, Lima R L, Malafronte A, Barros S F and Martins M N 2017 The 10–100 keV beam line of the São Paulo Microtron electron accelerator *Int. Forum on Advances in Radiation Physics (Buenos Aires, Argentine, 4–5 May 2017); Radiat. Phys. Chem.* accepted
[17] www.if.usp.br/lamfi/ (Accessed: 12 January 2017)
[18] Mayer M 1999 *AIP Conf. Proc.* **475** 541
[19] Silva T F, Rodrigues C L, Mayer M, Moro M V, Trindade G F, Aguirre F R, Added N, Rizzutto M A and Tabacniks M H 2016 *Nucl. Instrum. Methods* B **371** 86
[20] Seltzer S M 1981 *Nucl. Instrum. Methods* **188** 133
[21] Barros S F, Maidana N L, Fernández-Varea J M and Vanin V R 2017 *X-Ray Spectrom.* **46** 34
[22] Fernández-Varea J M, Jahnke V, Maidana N L, Malafronte A A and Vanin V R 2014 *J. Phys. B: At. Mol. Opt. Phys.* **47** 155201
[23] Krause M O and Oliver J H 1979 *J. Phys. Chem. Ref. Data* **8** 329
[24] Scholze F and Procop M 2009 *X-Ray Spectrom.* **38** 312
[25] Gao F, Campbell L W, Devanathan R, Xie Y L, Zhang Y, Peurrung A J and Weber W J 2007 *Nucl. Instrum. Methods* B **579** 292
[26] Deslattes R D, Kessler E G Jr, Indelicato P, Billy L, Lindroth E and Anton J 2003 *Rev. Mod. Phys.* **75** 35
[27] Scofield J H 1974 *At. Data Nucl. Data Tables* **14** 121

[28] Seltzer S M and Berger M J 1986 *At. Data Nucl. Data Tables* **35** 345

[29] Pratt R H, Tseng H K, Lee C M and Kissel L 1977 *At. Data Nucl. Data Tables* **20** 175
Pratt R H, Tseng H K, Lee C M and Kissel L 1981 *At. Data Nucl. Data Tables* **26** 477 (erratum)

[30] Kissel L, Quarles C A and Pratt R H 1983 *At. Data Nucl. Data Tables* **28** 381

[31] Redus H R, Huber A C and Sperry D J 2008 *IEEE Nuclear Science Conf. (NSS/MIC '08), pp 3416–20, October 2008.* p 3416

[32] Barros S F, Vanin V R, Malafronte A A, Maidana N L and Martins M N 2017 *J. Synchrotron Radiat.* submitted

[33] Helene O and Vanin V R 1993 *Nucl. Instrum. Methods* A **335** 227

[34] Kolbe M, Hönicke P, Müller M and Beckhoff B 2012 *Phys. Rev.* A **86** 042512

[35] Scofield J H 1974 *Phys. Rev.* A **9** 1041

[36] Rao P V 1972 *Phys. Rev.* A **5** 997

[37] Campbell J L and Wang J X 1989 *At. Data Nucl. Data Tables* **43** 281

[38] Madison D H and Merzbacher E 1975 *Atomic Inner-Shell Processes* ed B Crasemann (New York: Academic) pp 1–69

[39] Berezhko E G and Kabachnik N M 1977 *J. Phys. B: At. Mol. Phys.* **10** 2467